Hopf Solitons in Helical and Conical Backgrounds of Chiral Magnetic Solids

Robert Voinescu,[1,†] Jung-Shen B. Tai (戴榮身),[1,†] and Ivan I. Smalyukh[1,2,3,*]
[1]Department of Physics, University of Colorado, Boulder, Colorado 80309, USA
[2]Materials Science and Engineering Program, Soft Materials Research Center and Department of Electrical, Computer, and Energy Engineering, University of Colorado, Boulder, Colorado 80309, USA
[3]Renewable and Sustainable Energy Institute, National Renewable Energy Laboratory and University of Colorado, Boulder, Colorado 80309, USA

(Received 14 April 2020; accepted 6 July 2020; published 27 July 2020)

Three-dimensional topological solitons attract a great deal of interest in fields ranging from particle physics to cosmology, but remain experimentally elusive in solid-state magnets. Here we numerically predict magnetic heliknotons, an embodiment of such nonzero-Hopf-index solitons localized in all spatial dimensions while embedded in a helical or conical background of chiral magnets. We describe conditions under which heliknotons emerge as metastable or ground-state localized nonsingular structures with fascinating knots of magnetization field in widely studied materials. We demonstrate magnetic control of three-dimensional spatial positions of such solitons, as well as show how they interact to form moleculelike clusters and possibly even crystalline phases comprising three-dimensional lattices of such solitons with both orientational and positional order. Finally, we discuss both fundamental importance and potential technological utility of magnetic heliknotons.

DOI: 10.1103/PhysRevLett.125.057201

While one-dimensional topological solitons, like magnetic Néel and Bloch domain walls $\pi_1(\mathbb{S}^1) = \mathbb{Z}$, have been studied for nearly a century [1–3], their higher-dimensional analogs remain relatively elusive, consistent with the Derrick-Hobart theorem [4] applied to systems where solitons are unstable against rescaling perturbations. Evading predictions of the theorem, diverse embodiments of such high-dimensional solitons were found in nuclear physics, superconductors, liquid crystals, magnets, optics, and so on [5–20], with sources of stability ranging from high-order-derivative terms in the Skyrme model [21,22] and superconductors [23] to chiral terms in condensed matter [3,14–16]. In solid-state noncentrosymmetric magnets, the two-dimensional $\pi_2(\mathbb{S}^2) = \mathbb{Z}$ solitons, often called "baby skyrmions" to denote that they are lower-dimensional analogs of Skyrme's $\pi_3(\mathbb{S}^3) = \mathbb{Z}$ nuclear physics counterparts [3], are nowadays a major theme of fundamental and spintronics-inspired applied research [24,25]. However, the three-dimensional (3D) Hopf solitons, $\pi_3(\mathbb{S}^2) = \mathbb{Z}$ topological solitons localized in all three spatial dimensions [5,6], remain experimentally elusive in magnetic solids. Predictions of such solitons [8–10,26] embedded within the ferromagnetic background remain to be experimentally tested. On the other hand, individual and 3D crystalline lattices of Hopf solitons (called "heliknotons") were recently demonstrated in a helical background of cholesteric liquid crystals [17].

In this Letter, we predict heliknotons embedded in the helical and conical backgrounds of bulk chiral magnets. These heliknotons display Hopf-fibrationlike linking of preimages in the magnetization field $\boldsymbol{m}(\boldsymbol{r})$ and singular vortex lines forming links and knots in the nonpolar immaterial helical wave vector field $\boldsymbol{q}(\boldsymbol{r})$. We derive structural phase diagrams with (meta)stability of heliknotons by comparing their free energy to those of topologically trivial helical and conical states. We probe how stability of heliknotons is further controlled by experimentally accessible applied magnetic fields and magnetocrystalline anisotropies, which can arise due to crystal symmetry, mechanical stress, or lattice mismatches [27–29]. We show that the position and orientation of magnetic heliknotons can be effectively controlled in 3D and that emergent magnetic field lines also form Hopf-fibrationlike structures. Numerically simulated Lorentz transmission electron microscopy (LTEM) images have characteristic features that will guide experimental discovery of these topological solitons. Finally, we study heliknoton interactions and oligomeric self-organizations, suggesting the possibility of 3D crystalline phases.

We use the standard micromagnetic Hamiltonian of a chiral magnet with the energy density $w = w_i + w_Z + w_a$, where

$$w_i = \left(\frac{J}{2}(\nabla \boldsymbol{m})^2 + D\boldsymbol{m} \cdot (\nabla \times \boldsymbol{m})\right), \tag{1}$$

$$w_Z = -\mu_0 M_s \boldsymbol{m} \cdot \boldsymbol{H}. \tag{2}$$

w_i contains the Heisenberg exchange and Dzyaloshinskii-Moriya interaction terms with corresponding constants J

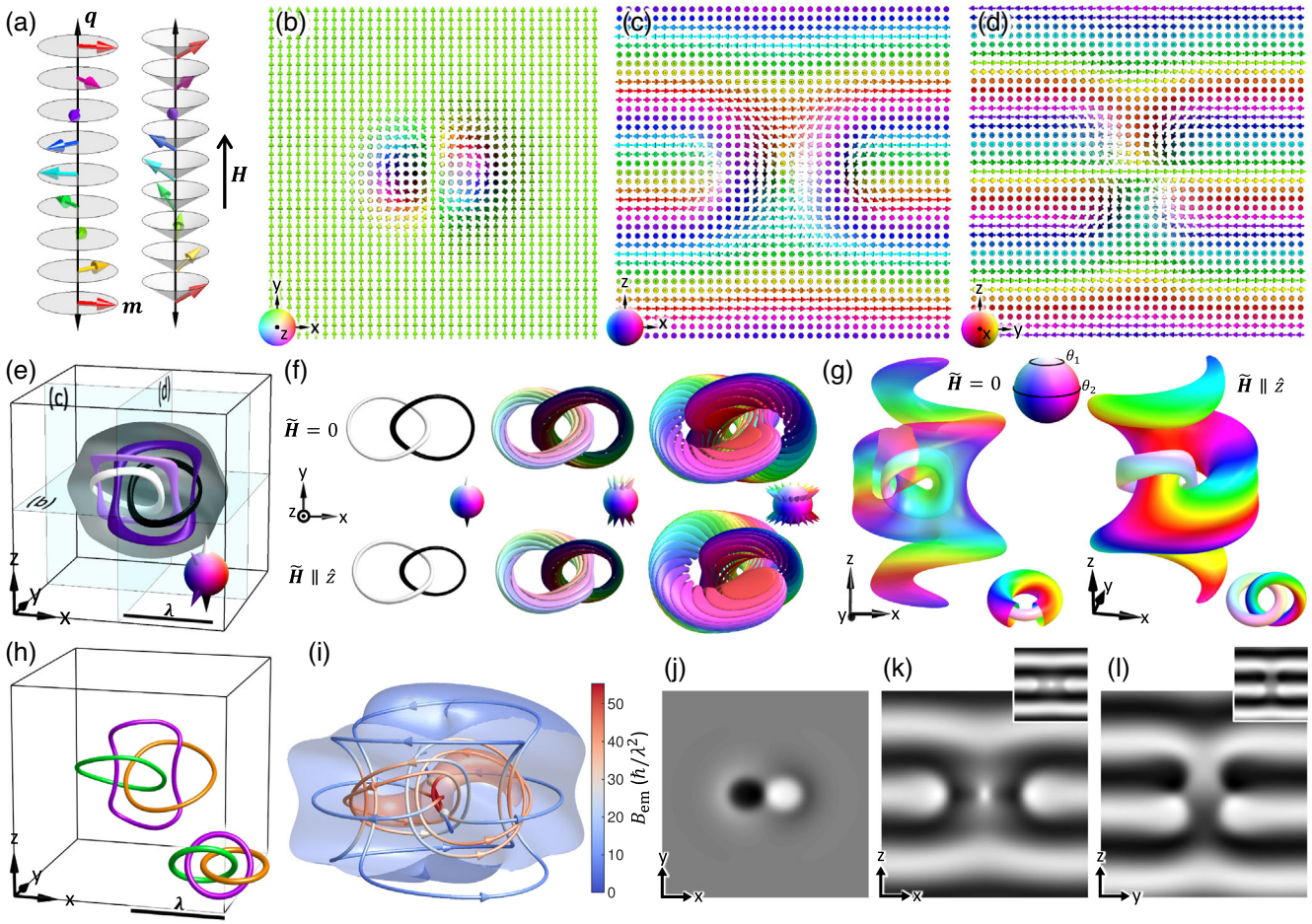

FIG. 1. Magnetic heliknoton. (a) Helical (left) and conical fields (right). (b)–(d) Simulated cross sections of $\boldsymbol{m}(\boldsymbol{r})$ of a heliknoton in a helical background. $\boldsymbol{m}(\boldsymbol{r})$ is shown with arrows colored according to orientations on $\mathbb{S}^2$ (bottom-left insets). (e) Preimages in $\boldsymbol{m}(\boldsymbol{r})$ of a heliknoton colored according to their orientations shown as cones on $\mathbb{S}^2$ (bottom-right inset). The gray isosurface (bisected for clarity) shows the region with small deviation of $\boldsymbol{q}(\boldsymbol{r})$ from the background $\boldsymbol{q}_0$. (f) Preimages of constant-polar-angle orientations as cones on $\mathbb{S}^2$ of heliknotons in a helical field (top, $\tilde{\boldsymbol{H}} = 0$) and in a conical field (bottom, $\tilde{\boldsymbol{H}} = 0.15\hat{z}$). (g) Constant-polar-angle surfaces at angles shown on $\mathbb{S}^2$ of heliknotons in a helical field (left, $\tilde{\boldsymbol{H}} = 0$) and in a conical field (right, $\tilde{\boldsymbol{H}} = 0.15\hat{z}$). Schematics of the nesting of tori surfaces are shown in the bottom-right insets. (h) Singular vortex lines in $\boldsymbol{q}(\boldsymbol{r})$ forming three mutually linked rings (schematic in bottom-right inset). (i) Visualization of $\boldsymbol{B}_{\text{em}}$ in a magnetic heliknoton by the isosurfaces colored by magnitude and streamlines with cones. (j)–(l) Simulated LTEM images of a heliknoton in (b)–(d) for different directions. Top-right insets in (k) and (l) show the images with the characteristic contrast of a heliknoton reduced in thick samples.

and D defining the helical wavelength $\lambda = 2\pi(J/D)$. w_Z is the Zeeman coupling term, where $\boldsymbol{H}$ is the applied field, M_s is the saturation magnetization, and μ_0 is the vacuum permeability. The magnetocrystalline anisotropy term is $w_a = -K_u(\boldsymbol{m}\cdot\hat{k})^2$ for uniaxial anisotropy and $w_a = -K_c(m_x^4 + m_y^4 + m_z^4)$ for cubic anisotropy, where K_u and $\hat{k}$ are the uniaxial anisotropy strength and axis, and K_c is the cubic anisotropy strength. To make our findings applicable to a broad range of materials (see Supplemental Material [30]), we use dimensionless fields and anisotropy strengths $\tilde{\boldsymbol{H}} = \boldsymbol{H}/H_D$ and $\tilde{K}_{u(c)} = K_{u(c)}/\mu_0 M_s H_D$, where $H_D = D^2/\mu_0 M_S J$ is the critical field along the helical axis that fully unwinds the helical state [30].

Adopting the field configuration of liquid-crystal heliknotons in Ref. [17] as the initial condition of $\boldsymbol{m}(\boldsymbol{r})$, we minimize free energy and find that the individual 3D-localized magnetic heliknotons in the bulk helical background at no fields or anisotropies [Figs. 1(a)–1(d)] as metastable states with energy $E_0 = 8.58J\lambda$ when taking the helical background state as the reference. Preimages of constant $\boldsymbol{m}(\boldsymbol{r})$ corresponding to $\mathbb{S}^2$ points are closed loops interlinking once with other individual preimages. This geometric analysis allows the assignment of the Hopf index $Q = 1$ to the heliknoton, which is consistent with the numerically calculated Q up to numerical error [8,35]. The spatial extent of a heliknoton can be visualized by the isosurface of a small deviation of $\boldsymbol{q}(\boldsymbol{r})$ from the uniform far

field $\boldsymbol{q}_0$ [Fig. 1(e)]. Preimages of $\mathbb{S}^2$ points of constant polar but different azimuthal angles form deformed tori nested around the preimages of north and south poles [Fig. 1(f)]. The two sets of nested tori are separated by the preimages of points on the equator of $\mathbb{S}^2$, representing the region occupied by the far field. In a heliknoton embedded in a helical background, preimage tori corresponding to points of the same latitude on either hemisphere of $\mathbb{S}^2$ intertransform by a π rotation along $\boldsymbol{q}_0$ with respect to the geometric center of the heliknoton. This symmetry is broken when a magnetic field is applied along $\boldsymbol{q}_0$ and the helical background transitions into the conical state with a cone angle $\theta_c = \cos^{-1}\tilde{H}$ [Fig. 1(a)]. As a result of such helical-to-conical transition in the far field, two preimage tori of polar angles θ_1 and θ_2 ($\theta_1 < \theta_c < \theta_2 < \pi/2$) transition from being both coaxial with the north pole's preimage to forming a noncoaxial link of preimage tori, with the overall $\pi_3(\mathbb{S}^2)$ topology of $\boldsymbol{m}(\boldsymbol{r})$ [Fig. 1(g)]. Thus, heliknotons can exist in a conical field background of varying cone angle, though we could stabilize heliknotons only up to $\tilde{H} \approx 0.2$. Beyond this field, the high-energy cost of regions with $\boldsymbol{m}(\boldsymbol{r})$ antiparallel to $\boldsymbol{H}$ overcomes the topological barrier, transforming the $Q = 1$ heliknoton to the topologically trivial conical state through nucleation and propagation of singular defects (Bloch points) [35].

While heliknotons are fully nonsingular structures in $\boldsymbol{m}(\boldsymbol{r})$, nontrivial topology characterizes not only this material field. Singular vortex lines in nonpolar $\boldsymbol{q}(\boldsymbol{r})$ form three mutually linked loops, different from the trefoil-knot vortices of liquid crystal heliknotons [17,30] [Fig. 1(h)]. We also calculate the emergent field $(B_{\mathrm{em}})_i \equiv \hbar\varepsilon^{ijk}\boldsymbol{m}\cdot(\partial_j\boldsymbol{m}\times\partial_k\boldsymbol{m})/2$, a fictitious field describing the interaction between conduction electrons and the underlying spin texture related to many spintronic implications [36]. $\boldsymbol{B}_{\mathrm{em}}$ correlates with the localized structure of $\boldsymbol{m}(\boldsymbol{r})$ and features closed-loop streamlines, with each pair of loops linked exactly once, once again resembling the Hopf fibration [Fig. 1(i)]. The topology of Hopf fibrations in $\boldsymbol{B}_{\mathrm{em}}$ streamlines in both magnetic heliknotons and hopfions (embedded in a helical and uniform background, respectively) is a salient feature of their $\pi_3(\mathbb{S}^2)$ topology in $\boldsymbol{m}(\boldsymbol{r})$ [8]. To facilitate experimental discovery of such magnetic heliknotons, we numerically simulate their LTEM images using energy-minimizing $\boldsymbol{m}(\boldsymbol{r})$ [Figs. 1(j)–1(l)], which significantly differ from those of other topological states found so far [19]. Recent advances in 3D imaging of $\boldsymbol{m}(\boldsymbol{r})$ could also assist in unambiguously showing their existence [37].

When a magnetic field $\boldsymbol{H}$ is applied perpendicular to $\boldsymbol{q}_0$, the helical state transforms from a harmonic modulation to distorted helicoids [38,39]. The energy of a heliknoton hosted within a distorted helicoidal background depends on the relative orientation of $\boldsymbol{H}$ and the orientation of a heliknoton defined by the magnetization $\boldsymbol{m}_h$ at its geometric center. At $\tilde{H} = 0.05$, heliknotons remain stationary

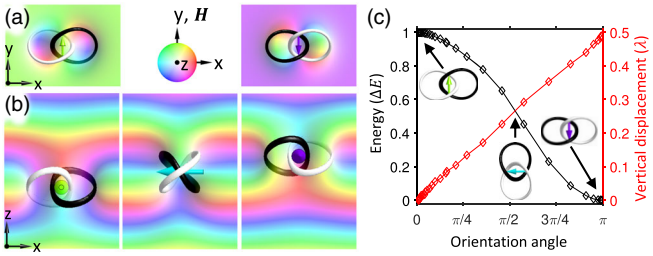

FIG. 2. Screw motions of heliknotons induced by external magnetic fields. (a) Heliknotons, visualized by preimages of poles, with orientations $\boldsymbol{m}_h$ parallel (left) or antiparallel (right) to the applied field being the metastable and stable state, respectively. (b) Screw motion of a heliknoton at $\tilde{\boldsymbol{H}} = 0.05\hat{y}$ relaxing from metastable parallel to stable antiparallel orientation. (c) The energy, orientation, and vertical displacement of a heliknoton relaxing from the metastable parallel configuration to the stable antiparallel configuration upon a perturbing magnetic field; the energy is normalized by $\Delta E = E_{\mathrm{parallel}} - E_{\mathrm{antiparallel}}$ and referenced by $E_{\mathrm{antiparallel}}$.

when $\boldsymbol{H}$ is either parallel or antiparallel to $\boldsymbol{m}_h$, while the energy difference between the former and the latter case is $\Delta E = 0.13\lambda J$, $E_{\mathrm{parallel}} = E_{\mathrm{antiparallel}} + \Delta E$ [Fig. 2(a)]. With the heliknoton being a metastable excitation within the helicoidal background, $\boldsymbol{H}$ parallel (antiparallel) to $\boldsymbol{m}_h$ expands (contracts) [Fig. 2(a)] the spatial extent of $\boldsymbol{m}(\boldsymbol{r})$ distortions. A small variation of the angle between $\boldsymbol{H}$ and $\boldsymbol{m}_h$ drives the heliknoton away from the metastable $\boldsymbol{m}_h \| \boldsymbol{H}$ state, and the heliknoton undergoes a screwlike motion of correlated rotation and displacement along $\boldsymbol{q}_0$ in a sense consistent with the material chirality, eventually arriving at the antiparallely-aligned state [Fig. 2(b)]. Figure 2(c) shows the heliknoton's energy difference versus orientation and the correlated vertical displacement during this motion. At fields as small as $\tilde{H} = 0.05$, heliknotons can be perturbed out of metastability when the angle between $\boldsymbol{H}$ and $\boldsymbol{m}_h$ is as small as 0.01°. At larger fields, a larger angle between $\boldsymbol{H}$ and $\boldsymbol{m}_h$ is required to drive the screw motion due to the adaptive deformation of $\boldsymbol{m}(\boldsymbol{r})$ and corresponding pinning of the heliknoton by $\boldsymbol{H}$. For $\boldsymbol{H} \perp \boldsymbol{m}_h$ and rotating synchronously with the screw motion of heliknotons, such rotating-wave magnetic field can be used to control orientations and positions of heliknotons (see Supplemental Material [30]).

We explore heliknoton stability at applied fields and various magnetocrystalline anisotropies by comparing free energy to that of topologically trivial helical (distorted helicoidal) and conical states (Fig. 3). The fields are collinear with $\boldsymbol{m}_h$ and take positive values when parallel to $\boldsymbol{m}_h$. We consider $|\tilde{H}| \leq 0.45$, beyond which significant stretching and distortion in the heliknotons take place. Three cases are considered: uniaxial easy-plane anisotropy with the hard-axis $\hat{k} \| \boldsymbol{q}_0$ [$K_u < 0$, Fig. 3(a)], uniaxial easy-axis anisotropy with the easy-axis $\hat{k} \perp \boldsymbol{q}_0$ and collinear with $\boldsymbol{H}$ [$K_u > 0$, Fig. 3(b)], and cubic anisotropy [Fig. 3(c)]. For uniaxial anisotropies, heliknotons are always higher

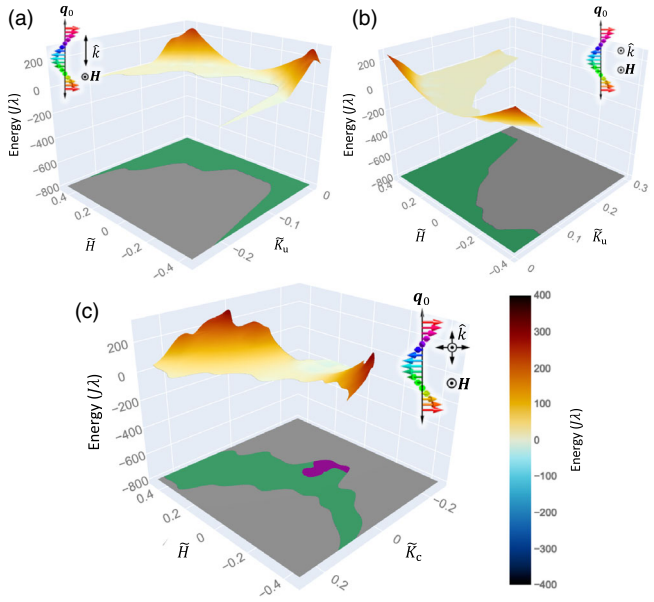

FIG. 3. Heliknoton stability. (a)–(c) Energy surfaces and stability diagrams of heliknotons in a chiral magnetic with (a) uniaxial easy-plane anisotropy, (b) uniaxial easy-axis anisotropy, and (c) cubic anisotropy. The energy is presented as the difference between the heliknoton energy and that of the minimum of helical and conical states. Colored regions indicate stable (purple), metastable (green), and unstable (gray) heliknotons. Relative orientations of $\boldsymbol{q}_0$, $\boldsymbol{H}$, and $\hat{k}$ are shown in the insets.

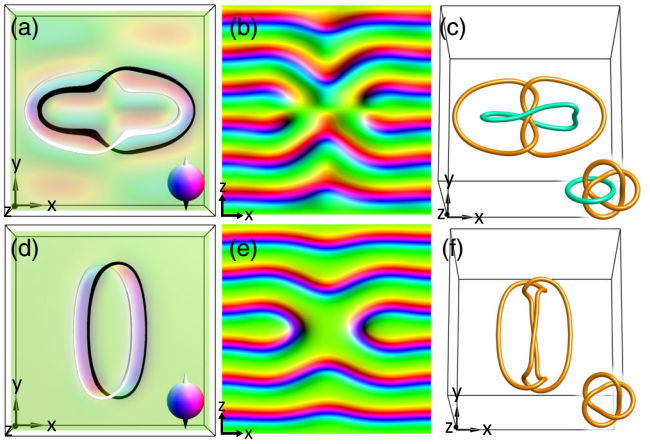

FIG. 4. Deformed heliknotons. (a)–(c) A heliknoton at $\tilde{\boldsymbol{H}} = 0.4\hat{y}$, shown using preimages of poles in $\mathbb{S}^2$ in (a) and $\boldsymbol{m}(\boldsymbol{r})$ colored according to orientations on $\mathbb{S}^2$ in midplane cross sections in (a) and (b), and singular vortex loops in $\boldsymbol{q}(\boldsymbol{r})$ in (c) shown by colored tubes. (d)–(f) A heliknoton at $\tilde{\boldsymbol{H}} = 0.45\hat{y}$ and easy-axis uniaxial anisotropy $\tilde{K}_u = 0.16$ along $\hat{y}$, shown by preimages of poles in (d) and $\boldsymbol{m}(\boldsymbol{r})$ colored according to orientations on $\mathbb{S}^2$ in midplane cross sections in (d) and (e) and singular vortex lines in $\boldsymbol{q}(\boldsymbol{r})$ in (f).

energy than the topologically trivial structures but persist as metastable states within a broad parameter range (colored green in Fig. 3). Within metastability regions, these solitons are often geometrically deformed by fields and anisotropies (Fig. 4) [30]. Interestingly, this stretching preserves topology and Hopf index but sometimes alters the singular vortex lines in the immaterial field $\boldsymbol{q}(\boldsymbol{r})$ (Fig. 4). The stretching occurs for both positive and negative $\boldsymbol{H}$, though it is more prevalent for antiparallel $\boldsymbol{H}$ and $\boldsymbol{m}_h$, providing a means for the geometric control of heliknotons. In the cases of easy-plane and easy-axis uniaxial anisotropies, the conical state with helical axis colinear with $\boldsymbol{H}$ is the lowest energy state at higher fields and the energy difference between heliknotons and conical states increases with $|\tilde{H}|$, yielding the valleylike energy surfaces along the field axis [Figs. 3(a) and 3(b)]. At stronger anisotropy strengths, easy-plane anisotropy tends to restore the helical state [Fig. 3(a)] and easy-axis anisotropy tends to unwind the twisted structures [Fig. 3(b)], both tending to destabilize heliknotons (gray areas in Fig. 3). The metastability range of heliknotons against strong uniaxial anisotropies is extended with the applied field strength, particularly in the case of positive fields ($\boldsymbol{H} \| \boldsymbol{m}_h \| \hat{y}$). This is because regions with $\boldsymbol{m}(\boldsymbol{r}) \| \boldsymbol{H}$ are anchored against the destabilizing uniaxial anisotropies, and the expansion induced by positive $\boldsymbol{H}$ helps counteract the shrinking of heliknotons during destabilization [Fig. 2(a)]. For cubic anisotropy with $K_c < 0$ (hard axes for $\langle 100 \rangle$ directions), heliknotons have energy even lower than that of the conical and helical states in some parameter region and are the globally stable state [colored purple in Fig. 3(c)]. This is a result of delicate competition between different free energy terms. At strong cubic anisotropy and $K_c > 0$, heliknotons become unstable, but they are also metastable within a broad range of parameters that correspond to widely studied material systems like MnSi, FeGe, Cu_2OSeO_3, etc., [18,27,40]. Interestingly, cubic anisotropy has also been reported to be critical for observing a novel solitonic state found at temperatures lower than that of the conventional A phase of skyrmions [27,41]. Our findings indicate that chiral magnetic materials with cubic anisotropy and $K_c < 0$ are the best candidates for observing magnetic hopfions of heliknoton type introduced here [Fig. 3(c)].

Heliknotons interact by sharing perturbations in the helical or conical background around them and minimizing the overall free energy of multisoliton configurations versus their relative 3D positions and orientations. Figures 5(a) and 5(b) show the positive (red) and negative (green) perturbations relative to the helical background energy density around an individual heliknoton in an isotropic chiral magnetic at no fields. Starting with two-heliknoton configurations with different orientations relative to the separation vector, heliknotons display anisotropic attractive interactions and can form three different dimer configurations [Fig. 5(c)] [30]. The energy per heliknoton for all dimer configurations is reduced as compared to that of an individual heliknoton E_0 as a result of sharing regions of high-energy $\boldsymbol{m}(\boldsymbol{r})$ distortions. The energy differences between different dimer configurations can be as small as $\Delta E_{23} = 0.045 J\lambda$ between dimer 2 and dimer 3, which, depending on material

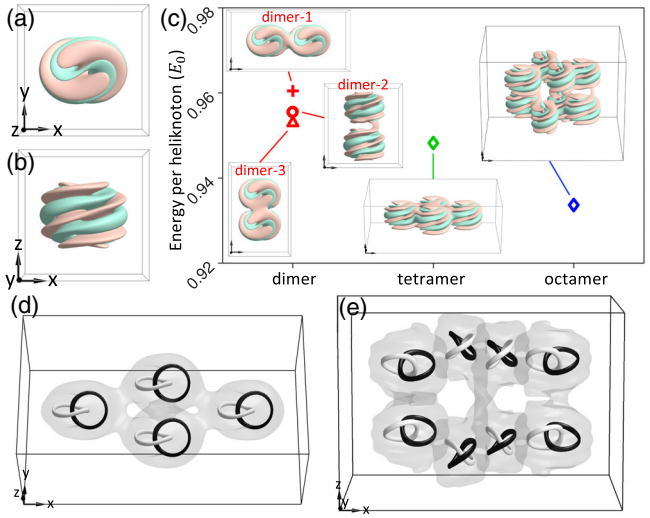

FIG. 5. Oligomeric assemblies of magnetic heliknotons. (a), (b) Isosurfaces of positive (red) and negative (green) perturbations in the background energy density by an individual heliknoton. (c) Energy per soliton of dimers, tetramer, and octamer, in units of E_0. Configurations of each oligomer are shown as insets. Tetramer (d) and octamer (e) of heliknotons shown by preimages at poles and isosurfaces of small deviation of $\boldsymbol{q}(\boldsymbol{r})$ from the background.

parameters, can be large ($\Delta E_{23}/k_BT \approx 10$ and $T = 200$ K for FeGe) or comparable ($\Delta E_{23}/k_BT \approx 0.7$ and $T = 25$ K for MnSi) to thermal energy (see Supplemental Material [30]). With the formation of tetramer and octamer configurations, the free energy per heliknoton is further reduced. Within the heliknoton oligomer, the isosurfaces of perturbation in $\boldsymbol{q}(\boldsymbol{r})$ of individual heliknotons join into a single surface and the overall Hopf index becomes the sum of that of the solitonic constituents [Figs. 5(d) and 5(e)]. Thus, a heliknoton oligomer resembles a single high-charge heliknoton molecule or, in a different analogy, a high-baryon-number nucleus [42]. The complex configuration of the stabilized octamer cannot be straightforwardly expected on the basis of dimer or tetramer configurations, suggesting that the emergent crystalline assemblies of heliknotons could be complex. A systematic study of all possible symmetries and lattice parameters, for different external fields and magnetocrystalline anisotropies, could potentially reveal the energy-minimizing assembly of various heliknoton crystals and potential solitonic condensed matter phases, again drawing an analogy to skyrmion crystals [5,6] and synthetic skyrmion crystals in certain superfluids [43], though such exploration is beyond the scope of this Letter.

To conclude, we have modeled metastable and stable heliknotons in the helical and conical backgrounds of bulk chiral magnetic materials. The demonstrated 3D localization and magnetic spatial control of Hopf solitons within the helical background, combined with the conventional control of dynamical topological solitons by spin currents [24,26], may provide a versatile set of tools and properties needed for spintronics applications. Formation of clustered heliknoton oligomers suggests the possibility of using high-charge heliknotons as information carriers or as building blocks of topological phases. Our findings call for the experimental discoveries of magnetic heliknotons based on their unique LTEM textures or using other imaging techniques.

We acknowledge funding from the U.S. Department of Energy, Office of Basic Energy Sciences, Division of Materials Sciences and Engineering, under Award No. ER46921, Contract No. DE-SC0019293 with the University of Colorado at Boulder. This work utilized the RMACC Summit supercomputer, which is supported by the NSF (Grants No. ACI-1532235 and No. ACI-1532236), the University of Colorado Boulder, and Colorado State University.

*Corresponding author.
ivan.smalyukh@colorado.edu
†These authors contributed equally to this work.

[1] P. M. Chaikin and T. C. Lubensky, *Principles of Condensed Matter Physics* (Cambridge University Press, Cambridge, England, 2000).
[2] S. Weinberg, *The Quantum Theory of Fields* (Cambridge University Press, Cambridge, England, 1995), Vol. 2, Chap. 22.
[3] J. H. Han, *Skyrmions in Condensed Matter* (Springer International Publishing, New York, 2017).
[4] G. H. Derrick, J. Math. Phys. (N.Y.) **5**, 1252 (1964).
[5] N. Manton and P. Sutcliffe, *Topological Solitons* (Cambridge University Press, Cambridge, England, 2004).
[6] Y. M. Shnir, *Topological and Non-Topological Solitons in Scalar Field Theories* (Cambridge University Press, Cambridge, England, 2018).
[7] P. Sutcliffe, Phys. Rev. Lett. **118**, 247203 (2017).
[8] J.-. B. Tai and I. I. Smalyukh, Phys. Rev. Lett. **121**, 187201 (2018).
[9] Y. Liu, R. K. Lake, and J. Zang, Phys. Rev. B **98**, 174437 (2018).
[10] P. Sutcliffe, J. Phys. A **51**, 375401 (2018).
[11] S. Tsesses, E. Ostrovsky, K. Cohen, B. Gjonaj, N. H. Lindner, and G. Bartal, Science **361**, 993 (2018).
[12] S. Das *et al.*, Nature (London) **568**, 368 (2019).
[13] L. Faddeev and A. J. Niemi, Nature (London) **387**, 58 (1997).
[14] P. J. Ackerman, R. P. Trivedi, B. Senyuk, J. van de Lagemaat, and I. I. Smalyukh, Phys. Rev. E **90**, 012505 (2014).
[15] P. J. Ackerman and I. I. Smalyukh, Phys. Rev. X **7**, 011006 (2017).
[16] P. J. Ackerman and I. I. Smalyukh, Nat. Mater. **16**, 426 (2017).
[17] J.-S. B. Tai and I. I. Smalyukh, Science **365**, 1449 (2019).
[18] S. Muhlbauer, B. Binz, F. Jonietz, C. Pfleiderer, A. Rosch, A. Neubauer, R. Georgii, and P. Boni, Science **323**, 915 (2009).
[19] X. Z. Yu, Y. Onose, N. Kanazawa, J. H. Park, J. H. Han, Y. Matsui, N. Nagaosa, and Y. Tokura, Nature (London) **465**, 901 (2010).

[20] X. Zhang, Y. Zhou, and M. Ezawa, Sci. Rep. **6**, 24795 (2016).
[21] T. H. R. Skyrme, Proc. R. Soc. A **262**, 237 (1961).
[22] G. S. Adkins, C. R. Nappi, and E. Witten, Nucl. Phys. **B228**, 552 (1983).
[23] F. N. Rybakov, J. Garaud, and E. Babaev, Phys. Rev. B **100**, 094515 (2019).
[24] A. Fert, V. Cros, and J. Sampaio, Nat. Nanotechnol. **8**, 152 (2013).
[25] X. Zhang, Y. Zhou, K. M. Song, T.-E. Park, J. Xia, M. Ezawa, X. Liu, W. Zhao, G. Zhao, and S. Woo, J. Phys. Condens. Matter **32**, 143001 (2020).
[26] X. S. Wang, A. Qaiumzadeh, and A. Brataas, Phys. Rev. Lett. **123**, 147203 (2019).
[27] A. Chacon, L. Heinen, M. Halder, A. Bauer, W. Simeth, S. Mühlbauer, H. Berger, M. Garst, A. Rosch, and C. Pfleiderer, Nat. Phys. **14**, 936 (2018).
[28] Y. Nii, T. Nakajima, A. Kikkawa, Y. Yamasaki, K. Ohishi, J. Suzuki, Y. Taguchi, T. Arima, Y. Tokura, and Y. Iwasa, Nat. Commun. **6**, 8539 (2015).
[29] S. X. Huang and C. L. Chien, Phys. Rev. Lett. **108**, 267201 (2012).
[30] See Supplemental Material at http://link.aps.org/supplemental/10.1103/PhysRevLett.125.057201 for additional figures and videos, details of numerical modeling, and material parameters, which include Refs. [31–34].
[31] R. Takagi, D. Morikawa, K. Karube, N. Kanazawa, K. Shibata, G. Tatara, Y. Tokunaga, T. Arima, Y. Taguchi, Y. Tokura, and S. Seki, Phys. Rev. B **95**, 220406(R) (2017).
[32] R. Tomasello, E. Martinez, R. Zivieri, L. Torres, M. Carpentieri, and G. Finocchio, Sci. Rep. **4**, 6784 (2015).
[33] R. Bott and L. W. Tu, *Differential Forms in Algebraic Topology* (Springer, New York, 1995).
[34] S. McVitie and M. Cushley, Ultramicroscopy **106**, 423 (2006).
[35] J.-S. B. Tai, P. J. Ackerman, and I. I. Smalyukh, Proc. Natl. Acad. Sci. U.S.A. **115**, 921 (2018).
[36] N. Nagaosa and Y. Tokura, Phys. Scr. **T146**, 014020 (2012).
[37] D. Wolf, N. Biziere, S. Sturm, D. Reyes, T. Wade, T. Niermann, J. Krehl, B. Warot-Fonrose, B. Büchner, E. Snoeck, C. Gatel, and A. Lubk, Commun. Phys. **2**, 87 (2019).
[38] E. A. Karhu, U. K. Rößler, A. N. Bogdanov, S. Kahwaji, B. J. Kirby, H. Fritzsche, M. D. Robertson, C. F. Majkrzak, and T. L. Monchesky, Phys. Rev. B **85**, 094429 (2012).
[39] M. N. Wilson, E. A. Karhu, D. P. Lake, A. S. Quigley, S. Meynell, A. N. Bogdanov, H. Fritzsche, U. K. Rößler, and T. L. Monchesky, Phys. Rev. B **88**, 214420 (2013).
[40] X. Z. Yu, N. Kanazawa, Y. Onose, K. Kimoto, W. Z. Zhang, S. Ishiwata, Y. Matsui, and Y. Tokura, Nat. Mater. **10**, 106 (2011).
[41] M. Halder, A. Chacon, A. Bauer, W. Simeth, S. Mühlbauer, H. Berger, L. Heinen, M. Garst, A. Rosch, and C. Pfleiderer, Phys. Rev. B **98**, 144429 (2018).
[42] C. Naya and P. Sutcliffe, Phys. Rev. Lett. **121**, 232002 (2018).
[43] A. Samoilenka, F. N. Rybakov, and E. Babaev, Phys. Rev. A **101**, 013614 (2020).